

Pressure drag of two-layer shallow-water flow at an inclined oceanic ridge, independent of velocity

Achim Wirth, Jan-Bert Flór

▶ **To cite this version:**

Achim Wirth, Jan-Bert Flór. Pressure drag of two-layer shallow-water flow at an inclined oceanic ridge, independent of velocity. 2018. hal-01709679

HAL Id: hal-01709679
https://hal.science/hal-01709679

Preprint submitted on 15 Feb 2018

HAL is a multi-disciplinary open access archive for the deposit and dissemination of scientific research documents, whether they are published or not. The documents may come from teaching and research institutions in France or abroad, or from public or private research centers.

L'archive ouverte pluridisciplinaire **HAL**, est destinée au dépôt et à la diffusion de documents scientifiques de niveau recherche, publiés ou non, émanant des établissements d'enseignement et de recherche français ou étrangers, des laboratoires publics ou privés.

Pressure drag of two-layer shallow-water flow at an inclined oceanic ridge, independent of velocity

A. Wirth* and J.B. Flor†

Univ. Grenoble Alpes, CNRS, LEGI, F-38000 Grenoble, France

(Dated: February 15, 2018)

Abstract

The drag in geophysical flows over topography is commonly modeled by a quadratic law. For a rotating fluid, we show that in the two-layer shallow-water approach, the pressure drag of a sub-critical flow around an inclined ridge is in good approximation independent of the flow speed. Numerical simulations results confirm this for a large range of Rossby numbers for both, barotropic and baroclinic flows approaching the ridge. The behavior is explained by the observation that for larger speeds the flow crosses the ridge at lower depth leading to a shorter path-length. As the frictional head loss is a product of the velocity and the path length, both compensate.

* achim.wirth@legi.cnrs.fr

† jan-bert.flor@legi.cnrs.fr

I. INTRODUCTION

In 1786 Du Buat [7] measured the pressure over the surface of an obstacle in a moving fluid and observed that the upstream pressure exceeds the pressure at the down-stream side of the obstacle. The difference was eventually explained with the pressure drag, a result then much used for navigation industry. More recently the role of topography and pressure drag in oceanic and atmospheric flows has been subject of discussion. For the dependence of the drag on the flow velocity, generally, the simple fact that the inertia is the product of mass and velocity is used. Since the mass of fluid encountering an obstacle is itself a linear function of velocity, a quadratic-drag law follows [19]. The law applies also to the frictional forces in a turbulent boundary layer. A considerable effort in all fields of fluid dynamics is devoted to the determination of the friction coefficient, taking the quadratic law for granted. In a homogeneous fluid, a current over topography is known to generate a vertical shear in the horizontal velocity field over a large depth. In rotating fluid flows that are dominated by the Coriolis force, however, this shear is confined to a thin boundary layer while the interior flow is depth independent and shows the formation of Taylor columns in accordance with the theory of Taylor Proudman [16], [20]. Supposing a dominantly horizontal motion, we question how the drag varies with the dominance of the Coriolis force expressed by the Rossby number. This drag depends on the large scale motion, and in addition, when multiple layers or a stratification are present, the baroclinic interaction of this large scale flow with other layers.

The understanding of drag and its parametrization is relevant for the modeling of many geophysical flows and in particular climate models. Some examples are the Antarctic Circumpolar Current (ACC) and its interaction with topography [13], [14]. But also smaller scale flows around ridges are relevant [21]. A ridge which is believed to have a strong influence on the thermohaline circulation in the ocean is the Reykjanes Ridge. It is a major topographic feature of the North-Atlantic Ocean south of Iceland, where the lower and the upper limp of the meridional overturning circulation (MOC) superpose. It influences the main paths followed by the two limbs of the MOC and is the gate towards the deep convection areas for the warm water masses of the upper limb. However, the temporal mean and variability of the structure of the flow along and over the ridge as well as the prevailing dynamical regimes are still poorly understood, and the governing dynamical processes

involved are not fully identified. About 50% of the warm to cold conversion associated with the MOC occurs in the Reykjanes Ridge area (see [6]), thus highlighting the importance of the flow dynamics around this ridge for climate. Despite this clear influence, the horizontal and vertical structure of the flow along and over the ridge and their variability are still incompletely documented and sometimes subject to controversy [11]. Recently, the atmospheric flow patterns around a ridge have been investigated to explain the increase of the summer near-surface temperatures over the northeast coast of the Antarctic Peninsula [15]. Their results from numerical and laboratory experiments suggests that a change from blocked flow around the ridge to flow over the ridge can explain the strong anomaly in local warming. Low amplitude climatic changes in weather patterns can lead to flow transitions around topographic features resulting in strong variations in the local climate. They suggest that such mechanisms could also be at work in other mountainous areas as for example the Alps.

There is a large body of literature about stratified flow over idealized topography in a rotating fluid, either in the context of wind over mountains or ocean flows over ridges, of which some are reviewed by [4] and [10]. The Shallow Water Model (SWM) has been used for the study of the flow around a spherical topography [17], [18], and continued with the effect of bottom friction [9]. A single-layer flow intersected a circular topography. The fore-aft asymmetry was broken by a hydraulic control over the topography followed by a hydraulic jump or flow separation at the topography. Both lead to eddy shedding in the wake. Though sub-critical flow was considered and frictional processes were discussed [9], the drag was not evaluated. Most related to the present study are the experiments on a uniform flow over a uniform ridge on the f-plane [12] reporting on the derivation of single layer flow over topography as a function of the Rossby number. To our knowledge, this type of flow has not further been investigated in very much detail.

In this paper, we consider two-layer flow over an inclined ridge that is extended in part of the domain (see Fig. 1), and as diagnostic, investigate the loss of momentum due to pressure drag. We use a two-layer Shallow Water Model (SWM) in the rotating frame (f-plane), and restrict our investigation to sub-critical flow, i.e. we eliminate hydraulic jumps and flow separation. Since the veracity of the integration of super-critical flow and hydraulic jumps depends on the parameterization of the non-hydrostatic process that are not explicitly resolved in the shallow water equations, the flow is no longer depth independent

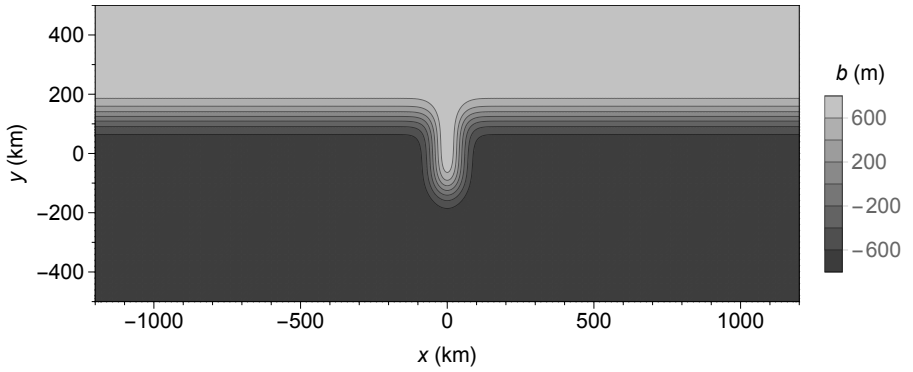


FIG. 1. Function b(x,y) from eq. (1) defining the bottom topography of the domain (m)

and vertical velocities are no longer small as compared to their horizontal counter parts, i.e. the basis of the shallow water approximation itself breaks down. For a strict investigation of super-critical flow and hydraulic jumps, fully three-dimensional models based on the Navier-Stokes equations should be used, which is out of the scope of the present study. The physical situation put forward to study the flow, the mathematical model adapted to its study and the corresponding numerical model are pre- sented in the next section, where we also discuss the conservation properties derived from the mathematical model. The numerical simulations and the obtained results are given in section III and discussed in section IV.

II. THE MODEL

A. The Physical Model

The physical model chosen to study the dynamics is a canal configuration which is $L_x = 2400$km long and $L_y = 1000$km wide. The depth is 2km plus/minus a topography, which is a continental shelf with a ridge as seen in Fig.1. The half-length of the ridge is $/L_r = 125$km, the e-folding thickness is $D_r = 60$km and the height is $B_r = 800$m. The analytic form of the topography is given by:

$$b(x,y) = B_r \left[\tanh\left(2(y'-1)\right)\left(1-e(x')\right) + \tanh\left(2(y'+1)\right)e(x')\right] \qquad (1)$$
$$\text{with} \quad e(x') = \exp\left(-x'^2\right) \quad \text{and} \quad x' = x/D_r, \quad y' = y/L_r$$

Two layers of different density fill the canal, with a reduced gravity $g' = g(\rho_2 - \rho_1)/\rho_2 = 2.0 \cdot 10^{-2}$, where g is the earth's gravitational constant. The subscript 1 and 2 denote the

upper and the lower layer, respectively. When the fluid is at rest the heavy water (ρ_2) extends from the bottom to a depth of 1km. The upper 1km is filled with the lighter water mass (ρ_1).

The dynamics is forced by damping towards a constant current along the topography in sponge layers at both ends of the channel. This forcing induces a current along the topographic slope. The mathematical detail of the forcing is given in the next subsection.

Note that no topographic feature penetrates into the upper layer, or equivalently the topography is always submerged by the lower layer. The vanishing of the lower layers thickness leads to super-critical flow, breaking of waves on the interface and increased mixing. Such phenomena are not explicitly foreseen in the shallow water model used here (see subsection II B). The dynamics of never vanishing layers allows to forgo implementing a parameterization of this process in the shallow water equations and facilitates the numerical solution (see subsection II D).

B. The Mathematical Model

The mathematical model we employ for this flow is the classical two-dimensional two-layer shallow water (SW) equations on the f-plane. Considering the model hierarchy, the SW equations include vortex stretching and Poincaré waves and are therewith more realistic than quasi-geostrophic or the 2D Navier Stokes equations, which neither include Poincaré waves.

The reference thicknesses in the two layers are h_i^0. The horizontal components of the vertically-averaged velocity vector are $u_i(t,x,y)$ (x-direction) and $v_i(t,x,y)$ (y-direction), where the index $(i = 1, 2)$ refers to respectively the upper and the lower layer. The deviation from a flat surface and interface is denoted by $\eta_1(t,x,y)$ and $\eta_2(t,x,y)$, respectively. Note that the total thickness of the upper layer is $h_1 = h_1^0 + \eta_1 - \eta_2$ and for the lower layer the thickness is $h_2 = h_2^0 + \eta_2 - b$. The writing of the equations is largely simplified if both symbols, h and η are used:

$$\partial_t u_1 + \quad u_1\partial_x u_1 + v_1\partial_y u_1 + g\partial_x \eta_1 - f v_1 = \nu\nabla^2 u_1 \tag{2}$$

$$\partial_t v_1 + \quad u_1\partial_x v_1 + v_1\partial_y v_1 + g\partial_y \eta_1 + f u_1 = \nu\nabla^2 v_1 \tag{3}$$

$$\partial_t \eta_1 + \partial_x\left[h_1 u_1\right] + \partial_y\left[h_1 v_1\right] + \partial_x\left[h_2 u_2\right] + \partial_y\left[h_2 v_2\right] = \kappa\nabla^2 \eta_1 \tag{4}$$

$$\partial_t u_2 + u_2\partial_x u_2 + v_2\partial_y u_2 + g''\partial_x \eta_1 + g'\partial_x \eta_2 - f v_2 = \nu\nabla^2 u_2 \tag{5}$$

$$\partial_t v_2 + u_2\partial_x v_2 + v_2\partial_y v_2 + g''\partial_y \eta_1 + g'\partial_y \eta_2 + f u_2 = \nu\nabla^2 v_2 \tag{6}$$

$$\partial_t \eta_2 + \partial_x \left[h_2 u_2\right] + \partial_y \left[h_2 v_2\right)] = \kappa\nabla^2 \eta_2 \tag{7}$$

Where $g = 10\text{ms}^{-2}$ is gravity, $g' = g(\rho_2 - \rho_1)/\rho_2 = g - g''$ and $g'' = g\rho_1/\rho_2$. The kinematic viscosity is given by ν. The boundary conditions at $y = \pm L_y/2$ are free-slip ($u = \partial_y v = 0$) for the velocity and there are no diffusive fluxes of layer thickness across the boundary. The boundary conditions at $x = \pm L_x/2$ are periodic. The Gent-McWilliams-parameter κ (Gent & McWilliams 1990, diffusion of layer thickness) is used in the same spirit as the viscosity parameter. Their role is to prevent the accumulation of energy/enstrophy at the smallest scales that are resolved numerically (see Frisch et al. 2008, for a detailed discussion of this bottleneck phenomena). The explicit value of the thickness-diffusion and the viscosity parameter depend on the resolution of the numerical model and the numerical scheme used.

There are sponge layers extending 200km in the x-direction at both ends of the canal. The dynamics is forced by restoring the free surface and the interface towards a prescribed value in the sponge layer:

$$\eta_i^{\text{sponge}} = l_i \frac{b}{B_r} \tag{8}$$

where b is the topography as defined in eq. 1 and the parameters l_i are varied between experiments. When $l_1 = l_2$ the forcing is barotropic.

The Reynolds number based on the lateral viscous dissipation is:

$$Re = \frac{u D_r}{\nu}. \tag{9}$$

An upstream baroclinic Froude number (based on the velocity in the lower layer relative to the maximal wave speed at the interface) is given by:

$$Fr = \frac{u_2^g}{\sqrt{g' h_e^0}}. \tag{10}$$

where we used the equivalent depth:

$$h_e^0 = \frac{h_1^0 h_2^0}{h_1^0 + h_2^0} \tag{11}$$

and u_2^g is the maximal geostrophic velocity imposed in the sponge layer. The barotropic Froude number is small in all experiments. The Rossby number is given by:

$$\epsilon = \frac{u_2^g}{D_r f}. \tag{12}$$

It compares the relative vorticity of the flow around the ridge to the planetary vorticity. Note that the vorticity around the ridge depends mainly on its width. A Burger number, which compares the stratification to rotation is $Bu = (\epsilon/Fr)^2$.

Due to the bottom topography the layer thickness of the lower layer varies from 200m to 1800m (when the fluid is at rest) so that the barotopic Rossby radius of deformation varies between $1100km \leq r_{bt} = \sqrt{g(h_1^0 + h_2^0)}/f \leq 1700km$ and a baroclinic radius of deformation between $18km \leq r_{bc} = \sqrt{g'h_e}/f \leq 32km$. In experiments eX05 (see table I) the Coriolis parameter and therefore also the Rossby radii are varied. A non-dimensional height of the topography given by $b' = \sqrt{g'b_0}/c_{bc} = \sqrt{(h_1^0 + h_2^0)b_0/h_1^0 h_2^0} \approx 1.26$ exceeds unity which means that the topography is high according to [15].

C. Pressure Drag

This subsection clarifies the notion of pressure drag in the frame of the SW equations and can easily be skipped by a reader familiar with this concept.

For the analysis of the influence of the ridge we consider the momentum M_i in the x-direction in each vertical layer in a rectangular domain that spans the entire width of the canal in the y-direction and from x_A to x_B in the x-direction ($A = [x_A, x_B] \times [y_A, y_B]$):

$$M_i = \rho_i \int_A u_i h_i da. \tag{13}$$

The momentum balance in the x-direction in the two layers, derived from eqs. (2) – (7), is given by:

$$\begin{aligned} \frac{1}{\rho_1}\partial_t M_1 = \int_A \partial_t(u_1 h_1) da = \left[\int_{y_A}^{y_B} u_1^2 h_1 dy\right]_{x_A}^{x_B} \\ + \int_A -g h_1 \partial_x \eta_1 + f h_1 v_1 \; da \\ - \int_A \nu h_1 \nabla^2 u_1 + \kappa u_1 \nabla^2 h_1 \; da \end{aligned} \tag{14}$$

$$\tag{15}$$

and

$$\frac{1}{\rho_2}\partial_t M_2 = \int_A \partial_t(u_2 h_2) da = -\left[\int_{y_A}^{y_B} u_2^2 h_2 dy\right]_{x_A}^{x_B} + \int_A -h_2\partial_x(g'\eta_2 + g''\eta_1) + f h_2 v_2 \; da - \int_A \nu h_2 \nabla^2 u_2 + \kappa u_2 \nabla^2 h_2 \; da \tag{16}$$

The first terms on the r.h.s of eqs. (14) and (16) represents the difference between the momentum transport entering the domain at x_A and leaving at x_B. The second line in both equations contains the accelerated mass due to the pressure gradient induced by variations of the surface (η_1) and the interface (η_2). They form a total integral if there exists a function so that $h_1 = F_1(\eta_1)$ and a function so that $h_2 = F_2(g'\eta_2 + g''\eta_1)$, which is the case when Bernoulli potentials exist. Note that when the flow is in geostrophic equilibrium we have:

$$v_1 = \frac{g}{f}\partial_x \eta_1 \;\text{ and }\; v_2 = \frac{g''}{f}\partial_x \eta_1 + \frac{g'}{f}\partial_x \eta_2 \tag{17}$$

and the Coriolis term (the second term of the surface integral) in both equations cancels the potential terms. This is explained by the fact that in a geostrophic flow differences in surface and isopycnal height do not lead to acceleration, as the pressure gradient is balanced by the Coriolis force. The value of the domain integral in the second line of eqs. (14) and (16) can thus be used to measure the departure from geostrophy in the domain. In the above equations the lower boundaries of the two layers do not appear explicitly and one might falsely conclude that they are not important for the momentum balance. The lower boundaries do modify both, the transport in the layers and shape of the upper boundary. This becomes apparent when hydrostacy is used and the momentum balance is evaluated based on the pressure at the lower boundaries of each layer. In this case the pressure drag exerted by the upper layer on the interface is

$$D_i = g\rho_1 \int_A h_1 \partial_x \eta_2 \, da, \tag{18}$$

and the pressure drag exerted by the upper layer and the lower layer on the topography:

$$D_b = g \int_A (\rho_1 h_1 + \rho_2 h_2)\partial_x b \, da = D_{b1} + D_{b2} \tag{19}$$

appears in the equations. The pressure terms used in eqs. (14) and (16) can be expressed

as:

$$g\int_A h_1\partial_x\eta_1 da = g\left[\int_{y_A}^{y_B}\frac{h_1^2}{2}\right]_{x_A}^{x_B} dy + D_i \tag{20}$$

$$\rho_2\int_A h_2\partial_x(g'\eta_2 + g''\eta_1)da = g\left[\int_{y_A}^{y_B}(\rho_2\frac{h_2}{2}dy + \rho_1 h_1)h_2 dy\right]_{x_A}^{x_B} - D_i + D_b. \tag{21}$$

The first terms in the above equations represent the acceleration due to differences in the layer thickness at the two boundaries of the canal. The second terms represent the pressure drag (also called "form drag") on the interface and third term in the second equation represents the bottom drag due to the surface and interface inclination. Note that if the densities and velocities in the two layers are equal we obtain the one-layer solution.

As in the case of d'Alembert's paradox [2] it is friction and time-dependence that bring the pressure gradient out of phase with the topography and allow for the existence of a pressure drag.

D. Numerical Model

The numerical model chosen to solve the above detailed mathematical model is a second-order-in-time Runge-Kutta scheme. The spatial discretisation is a centered second order in space scheme (first order at the boundary). The resolution is $\Delta x = \Delta y = 2km$ (1200×500 points) in space and $\Delta t = 1s$ in time. The short time-step is imposed by the barotropic gravity wave speed. The spatial resolution is $2km$ in both horizontal directions. The friction parameters adapted for this resolution and the time-stepping scheme are $\nu = \kappa$ ($\mathrm{m^2 s^{-1}}$).

Using even higher resolutions might not add much to our understanding of the physics involved as the approximations (*e.g.* hydrostatic-approximation) at the basis of the shallow water model are no longer valid for dynamical phenomena that have horizontal extensions comparable to the water depth (2km). Even higher resolution might teach us things about the mathematics of the SW model but not about the physics of the ocean.

Note also, that thethickness of the layers never vanishes, meaning that no numerical scheme to treat the processe is needed.

During spin-up of 100days the flow is forced not only in the sponge layers, but also in the interior. After that, the dynamics rapidly converges to an almost stationary state which is analyzed after 150days.

Using an explicit free surface model clearly slows down the numerical integration as compared to rigid-lid or implicit-free-surface schemes. But in the present work we investigate the pressure due to the combined surface and interface dynamics and they should therefore be solved in the most veracious way.

E. Experiments performed

Results from 20 numerical experiments are presented here. The experiments vary by strength of forcing, baroclinicity, horizontal viscosity and the Coriolis parameter (see table I).

As mentioned above, the time and space dependent (barotropic and baroclinic) Froude number is sub critical ($F < 1$) at all locations and times.

III. RESULTS

A. Description

All flows discussed here are almost time independent and close to geostrophy. A flow which is in geostrophic equilibrium is completely described by the pressure gradient created by the free surface and the interface. A strong (almost perfect) fore-aft symmetry is observed for both layers. The ridge leaves a strong imprint also in the dynamics of the upper layer, although the ridge is always submerged in the lower layer only, it modifies the interface between the two layers. In Fig. 2 we see that the path in the lower layer extends further along the ridge showing that the dynamics above the ridge is baroclinic.

There is a localized signal of weak Poincaré waves above the ridge. These Poincaré waves are modified by: (i) the variation in the layers thicknesses due to the topography and the variation of the interface; (ii) the vortical current in both layers. Above the topography the relative vorticity is negative and so the absolute vorticity is lower than the Coriolis parameter allowing for Poincaré waves with a frequency below the Coriolis parameter. Away from the ridge the waves are evanescent.

The dynamics is close to time independent. As the diffusive terms are small, potential vorticity, defined as $q_i = (\zeta_i + f)/h_i$ is almost conserved along the flows in both layers so

exp	l1	l2	f (10^{-4})	ν	ϵ	Re
e001	0.1	0.1	1.	100.	0.016	40
e002	0.25	.25	1.	100.	0.04	100
e003	0.5	0.5	1.	100.	0.08	200
e004	0.75	.75	1.	100.	0.12	300
e005	1.0	1.0	1.	100.	0.16	400
e006	1.5	1.5	1.	100.	0.24	600
e007	2.0	2.0	1.	100.	0.32	800
e012	0.25	.25	1.	200.	0.04	50
e013	0.5	0.5	1.	200.	0.08	100
e015	1.0	1.0	1.	200.	0.16	200
e017	2.0	2.0	1.	200.	0.32	400
e025	1.0	1.0	1.	50.	0.16	800
e105	1.0	1.0	2.	100.	0.04	200
e205	1.0	1.0	3.	100.	0.01778	133
e305	1.0	1.0	4.	100.	0.01	100
e1001	0.1	0.1 λ	1.	100.	0.032	80
e1002	0.1	0.25 λ	1.	100.	0.056	140
e1003	0.1	0.5 λ	1.	100.	0.096	240
e1005	0.1	1.0 λ	1.	100.	0.176	440
e1006	0.1	1.05 λ	1.	100.	0.184	480

TABLE I. Parameters varied between numerical experiments with the values of l_i present the forcing in the sponge layers, see eq. (8), $\lambda = g/g' = 500$ and non-dimensional parameters (based on the values in the sponge layer) associated.

that:

$$\vec{u_i} \cdot \nabla q_i = 0. \tag{22}$$

For small Rossby number (eq. (12)) (i.e. the relative vorticity is small compared to the Coriolis parameter) the flow turns around the topography in the lower layer. For larger

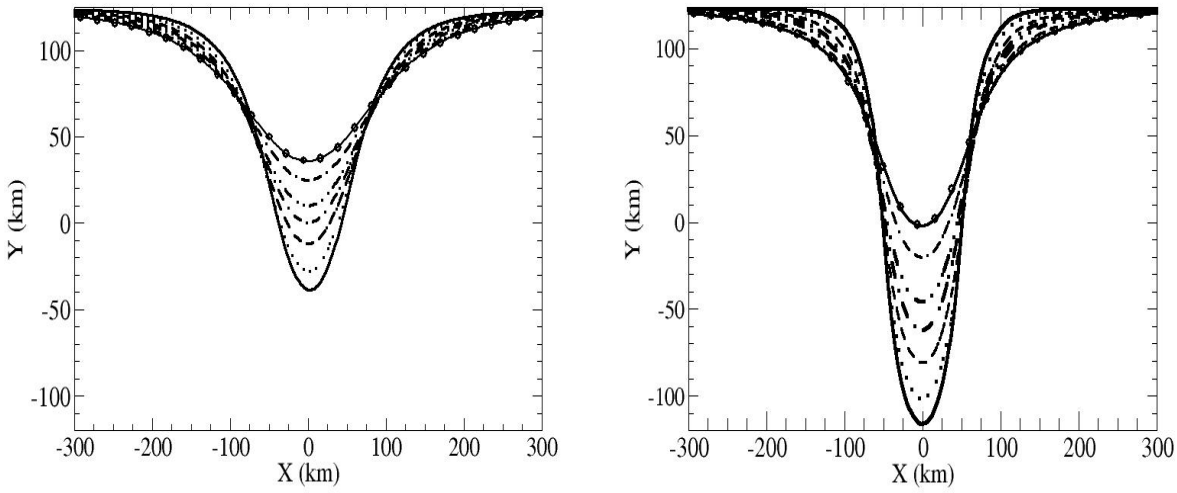


FIG. 2. Paths of the center of the current in the upper layer (left) and the lower layer (right) for e001 (—), e002 ($\cdots$), e003 ($- - -$), e004 ($\cdot - \cdot$), e005 ($- \cdot \cdot -$), e006 ($\cdot - - \cdot$), e007 (-⊖-). Higher Rossby-number flows show a smaller deviation of the flow by the topography.

Rossby numbers the relative vorticity becomes more important and is negative at the tip of the topography. To compensate the reduction of total vorticity ($\zeta_i + f$) the layer thickness decreases as the flow crosses the ridge further above the topography. Since the flow performs a less pronounced bend around the topography this leads at the same time to a decrease of the relative vorticity. This is clearly visible in Fig. 2 where the path of the centre of the current ($y = c(x)$) around the ridge in the two layers is shown for different Rossby numbers. The center of the current is determined by the constant potential vorticity $q_i(x, c(x)) = f/h_i^0$ in both layers. In Fig. 3 the y-coordinate of the center of the current above the ridge ($c(0)$) is given as a function of the Rossby number for both layers.

Since the variation in the topography influences the interface deviation the Froude number also plays a role for the path of the current. The effect of different Froude number on the path is found to be small for the lower layer. When comparing the ridge crossing for experiments with the same Rossby number and different Froude number (Fig. 3, right) only a small difference is seen (dotted and straight line almost superpose). The same does not apply to the current around the ridge in the upper layer (Fig. 3, left), for which the Froude number has a strong effect. The interface deviation in all experiments with a barotropic forcing

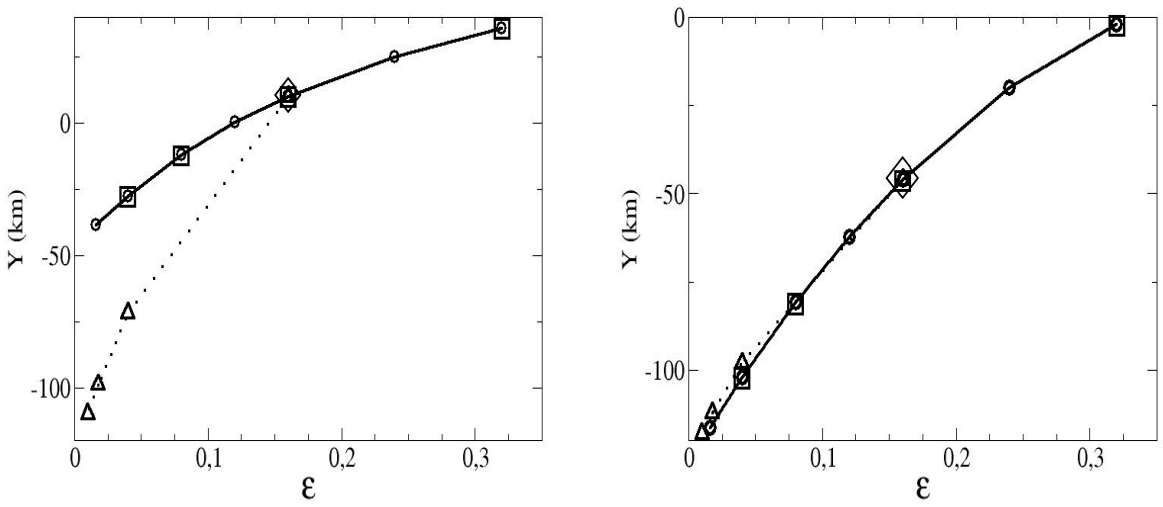


FIG. 3. y-coordinate of ridge crossing as a function of the Rossby number (ϵ) for the upper layer (left) and the lower layer (right), for different series of experiments: e00X ($\circ$), e01X ($\Box$), e025 ($\diamond$), eX05 ($\triangle$)

shows almost the same spatial distribution, except that the amplitude changes.

Comparing the series of experiments e00X to e01X and exp025, we see that viscosity, varied within the range chosen, has to leading order no influence on the path of the current ($\circ$, $\Box$ and $\triangle$ in Fig. 3 fall on almost the same line).

When the Coriolis parameter is increased, the path in the upper-layer approaches the path in the lower layer, which is a manifestation of Taylor-Proudman-Poincaré Theorem. This is clearly visible in Fig. 3 where the crossing of the ridge in the upper layer approaches the location of the crossing in the lower layer when the Burger number ($= (\epsilon/Fr)^2$) decreases, and the flow becomes more barotropic.

B. Pressure Drag

We have seen in the previous subsection, that to leading order the velocity field does not depend on the value of the chosen viscosity. In a non frictional and stationary case a Bernoulli potential exists and the flow around the symmetrical ridge is completely symmetrical and the pressure drag therefore vanishes. This is d'Alembert's paradox [8], [5] applied to the

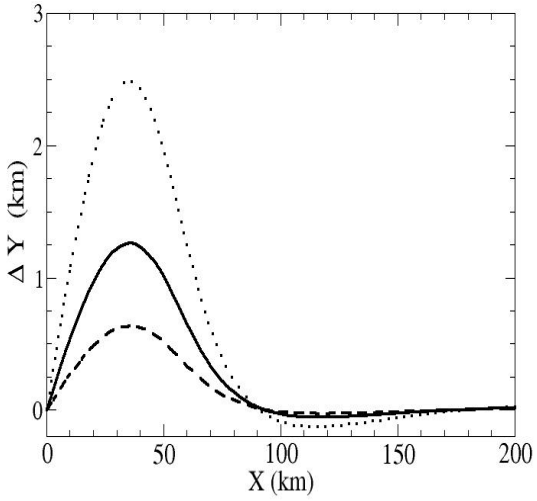


FIG. 4. Asymmetry in the y-component of path of the current across the ridge ($\Delta Y(x) = Y(x) - Y(-x)$) for e005 (—), e015($\cdots$) and e025 ($---$). When devided by the respective viscosity value (see Tab. I curves superpose.

flow around a symmetric ridge.

When considering the path of the flow around the ridge we can observe a slight asymmetry across the ridge, as depicted in Fig. 4, which is proportional to the viscosity. It is a measure of the frictional head-loss and is almost proportional to the viscosity value, the velocity (linear friction) and the path length. As we have seen in the previous section, a stronger flow leads to a shorter path length so that the pressure drag is, in the case considered here, almost independent of the Rossby number for values of $\epsilon > 0.1$.

For our analysis we consider the quantities defined in eq. (19) divided by the surface area and the density in the upper layer (ρ_1)(units $\mathrm{m^2 s^{-2}}$). The total pressure drag (D_b) and the pressure drag due to the interface (D_{b2}) for the experiments e00X are given in Fig. 5, the difference between the two curves is the pressure drag due to the surface (D_{b1}) . Results of e025 and e01X (not shown) perfectly superpose on these results when all are divided by the corresponding viscosity value, demonstrating that the pressure drag is a linear function of the friction parameter for the range of friction parameters considered here. Note, that the pressure drag due to the interface slightly decreases with increasing Rossby number, for Rossby numbers higher then $\epsilon = 0.12$.

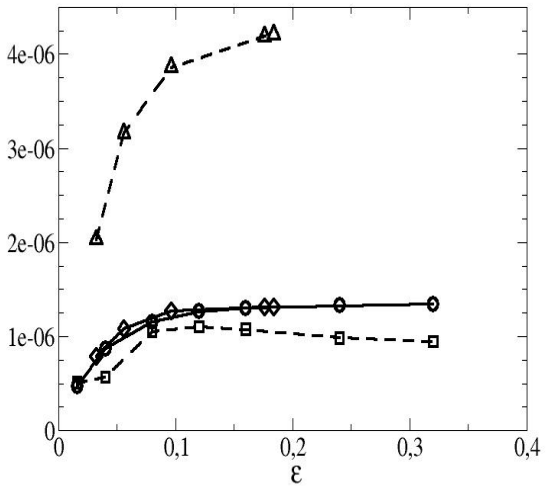


FIG. 5. Pressure drag (divided by the surface area and the density in the upper layer ρ_1, units $\mathrm{m}^2\mathrm{s}^{-2}$ integrated from $x = -120$km to $x = 120$km, see text) as a function of the Rossby number (ϵ). Total pressure drag (D_b) of exp00X ($\circ$) and exp100X ($\diamond$) and pressure drag due to the interface (D_{b2}) of exp00X ($\square$) and exp100X ($\triangle$).

For the experiments with baroclinic forcing (e100X) the total pressure drag is almost identical to the barotropic forcing when plotted as a function of the Rossby number in the lower layer (see Fig. 5. The pressure drag due to the interface is however five-fold higher but it is then compensated by a negative pressure drag due to the surface elevation.

IV. DISCUSSION AND CONCLUSION

We have studied a sub-critical flow around a ridge in a two layer configuration, with small dissipative processes having only a weak effect on the cross-stream structure of the flow along its path. The path of the current at the ridge in both layers is well described by the conservation of potential vorticity in both layers.

It is found that even though the dissipation is weak, it leads to a fore-aft asymmetry of the flow with respect to the ridge. This results in a pressure drag which depends only weakly (see Fig. 5) on the Rossby number for a substantial range of Rossby numbers ($\epsilon > 0.1$). This can be explained by the decreasing path-length of the fluid across the ridge, with increasing

Rossby number, and is a consequence of the (to leading order) conservation of potential vorticity in the weak dissipative cases considered here. Since the total drag is the sum of the frictional drag and the pressure drag, the former depends linearly on the path-length and the fluid velocity, i.e. a longer-path and a larger velocity results in a larger frictional drag across the ridge.

A velocity independent pressure drag has so far not been noticed in the context of flow-topography interaction, probably since previous investigations focused on strait ridges. The behavior is remarkably robust: for a baroclinicly forced flow almost identical results are obtained for the total pressure drag. This and the fact that the findings are explained by the conservation of potential vorticity suggest that our results are more than a curiosity in geophysical fluid dynamics. Previous investigations [12] have focused on strait ridges, we show that the case of an inclined ridge gives rise to new behaviors at large scales. Our results based on the (almost) conservation of potential vorticity also suggest that the drag depends on the precise representation of the inclination of the ridge. Other inclinations and forms will not only change the friction parameters, but also the friction law.

Similar results with the drag being independent of the flow speed, are obtained for flows over flexible objects such as plants [3], low Reynolds number flow of DNA molecules [22] and for objects moving in granular media [1]. Here the reduction of the path-length across the ridge with increasing speed can be considered as an analogue to the increased bending of a flexible object, both reducing the influence of the obstruction in the flow and lessen the drag.

Although the configuration is highly idealized, analytic solutions are not straightforward to deduce, as the presence of very low-amplitude trapped-Poincaré-waves confirms.

Our results apply also to atmospheric flows around mountain ridges, if they are large enough so that the Rossby number is around unity or smaller. The width of our ridge (120km) is small compared to the grid-size of most numerical models used to simulate the ocean dynamics in climate models. Its important effect on the flow dynamics suggests therefore that its parameterization in those models is relevant.

ACKNOWLEDGMENTS

We are grateful to the members of the RREX group for discussion. This paper is a contribution to the RREX project supported by IFREMER, CNRS and the French National Program LEFE coordinated by INSU and by a grant from Labex OSUG@2020 (Investissements d'avenir ANR10 LABX56).

[1] Albert , R., Pfeifer , M. A., Barabasi, A.-L., Schiffer , P., 1999, Slow drag in a granular medium. Phys. Rev. Lett. 82, 205.

[2] D'Alembert, Jean le Rond, 1768, Paradoxe proposé aux géomètres sur la résistance des fluides, in Opuscules mathématiques, 5 (Paris), Memoir XXXIV,xI, 132–138.

[3] Barois, T. and De Langre, E. 2013, Flexible body with drag independent of the flow velocity. J. of Fluid Mech., 735, R2. doi:10.1017/jfm.2013.516

[4] Boyer, D.L. and Davies, P.A., 2000, Laboratory Studies of Orographic Effects in Rotating and Stratified Flows, Ann. Rev. of Fluid Mech. 32, 165-202

[5] Darrigol, O., (2008), *Worlds of flow: A history of hydrodynamics from the Bernoullis to Prandtl*, OUP Oxford 372pages ISBN-13: 978-0199559114

[6] Desbruyères, D., V. Thierry, H. Mercier, (2013), Simulated decadal variability of the meridional overturning circulation across the A25-Ovide section. J. Geophys. Res., DOI: 10.1029/2012JC008342.

[7] Du Buat, P.L. G. (1786), Principes D'Hydraulique, Imprimerie de Monsieur

[8] Grimberg, G., Pauls, W. and Frisch, U. (2008), Genesis of dAlemberts paradox and analytical elaboration of the drag problem. Physica D: Nonlinear Phenomena, 237(14), 1878-1886.

[9] Grubisic, V., Smith, R. B., & Schär, C. (1995), The effect of bottom friction on shallow-water flow past an isolated obstacle. J. of atmos. sciences, 52, 1985-2005.

[10] van Heijst, G.J.F. & H.J.H. Clercx, H.J.H. (2009), Laboratory Modeling of Geophysical Vortices, Ann. Rev. of Fluid Mech. 41, 143-164.

[11] Lherminier, P., H. Mercier, T. Huck, C. Gourcuff, F. F. Perez, P. Morin, A. Sarafanov, (2010), The Atlantic Meridional Overturning Circulation and the subpolar gyre observed at the A25-OVIDE section in June 2002 and 2004. Deep Sea Res. I, doi:10.1016/j.dsr.2010.07.009.

[12] Maxworthy, T. (1977) Topographic Effects in Rapidly-rotating Fluids: Flow Over a Transverse Ridge J. of Applied Math. and Phys. (ZAMP) 28, 853–864.

[13] Olbers, D., (1998), Comments on On the Obscurantist Physics of Form Drag in Theorizing about the Circumpolar Current, J. Phys. Oceanogr., 28, 16471654.

[14] Olbers D., Borowski, D., Vlker, C. & Wolff J.-O. (2004) The dynamical balance, transport and circulation of the Antarctic Circumpolar Current. Ant. Sci. 4, 439470. doi:10.1017/S0954102004002251.

[15] Orr, A., G. J. Marshall, J. C. R. Hunt, J. Sommeria, C.-G. Wang, N. P. M. van Lipzig, D. Cresswell, John C. King (2007), Characteristics of Summer Airflow over the Antarctic Peninsula in Response to Recent Strengthening of Westerly Circumpolar Winds, J. Atmos. Sci., 65, 13961413. doi: http://dx.doi.org/10.1175/2007JAS2498.1

[16] Proudman, J. (1916), "On the motion of solids in a liquid possessing vorticity. Proc. R. Soc. Lond. A. 92, 408424. doi:10.1098/rspa.1916.0026.

[17] Schär, C. & Smith, R. B. (1993), Shallow-water flow past isolated topography. Part I: Vorticity production and wake formation. J. of atmos. sciences, 50, 1373-1400.

[18] Schär, C. & Smith, R. B. (1993), Shallow-water flow past isolated topography. Part II: Transition to vortex shedding. J. of atmos. sciences, 50, 1401-1412.

[19] Stull, R. (1988), An Introduction to Boundary Layer Meteorology Kluwer Academic Publishers, 1988, 666 p.

[20] Taylor, G.I. (1917), Motion of solids in fluids when the flow is not irrotational. Proc. R. Soc. Lond. A. 93, 92113. doi:10.1098/rspa.1917.0007.

[21] Warner, S.J. & MacCready, P. (2009), Dissecting the Pressure Field in Tidal Flow past a Headland: When Is Form Drag Real?. J. Phys. Oceanogr., 39, 29712984.

[22] Wirtz , D. (1995), Direct measurement of the transport properties of a single DNA molecule. Phys. Rev. Lett. 75, 2436.